Nanowires Framework Supported Porous Lotus-Carbon Anode Boosts Lithium-Ion and Sodium-Ion Batteries

Xiaochen Sun, Xuan Gao, Zhuo Li, Xin Zhang, Xiaoli Zhai, Qiuxia Zhang, Liuan Li,*
Nan Gao,* Guanjie He,* and Hongdong Li*

The novel design of carbon materials with stable nanoarchitecture and optimized electrical properties featuring simultaneous intercalation of lithium ions (Li$^+$) and sodium ions (Na$^+$) is of great significance for the superb lithium–sodium storage capacities. Biomass-derived carbon materials with affluent porosity have been widely studied as anodes for lithium-ion batteries (LIBs) and sodium-ion batteries (SIBs). However, it remains unexplored to further enhance the stability and utilization of the porous carbon skeleton during cycles. Here, a lotus stems derived porous carbon (LPC) with graphene quantum dots (GQDs) and intrinsic carbon nanowires framework (CNF) is successfully fabricated by a self-template method. The LPC anodes show remarkable Li$^+$ and Na$^+$ storage performance with ultrahigh capacity (738 mA h g^{-1} for LIBs and 460 mA h g^{-1} for SIBs at 0.2 C after 300 cycles, 1C≈372 mA h g^{-1}) and excellent long-term stability. Structural analysis indicates that the CNFs-supported porous structure and internal GQDs with excellent electrical conductivity contribute significantly to the dominant capacitive storage mechanism in LPC. This work provides new perspectives for developing advanced carbon-based materials for multifunctional batteries with improved stability and utilization of porous carbon frameworks during cycles.

X. Sun, Z. Li, X. Zhang, X. Zhai, Q. Zhang, L. Li, N. Gao, H. Li
State Key Lab of Superhard Materials
College of Physics
Jilin University
Changchun 130012, P. R. China
E-mail: 1615851970@qq.com; liliuan@jlu.edu.cn; gaon@jlu.edu.cn; hdli@jlu.edu.cn
X. Gao, G. He
Christopher Ingold Laboratory
Department of Chemistry
University College London
London WC1H 0AJ, UK
E-mail: g.he@ucl.ac.uk

1. Introduction

Li-ion batteries (LIBs) have been widely used in portable electronic devices owing to their high energy density and extended lifespan. However, the cost and safety concerns related to large-scale commercial production of LIBs could become significant challenges in the future.[1] In this regard, sodium-ion batteries (SIBs) are a promising alternative to LIBs, as they exhibit similar electrochemical properties while being more cost-effective and having abundant resources than LIBs.[2] However, the electrode materials for SIBs tend to show poorer insertion kinetics and lower capacity than those for LIBs due to the heavier atomic mass and larger ionic radius.[3] Among numerous electrode materials (such as alloys, silicon, metal oxides, carbon, etc.[4–6]) few anode materials can be suitable host materials to accommodate both lithium ion (Li$^+$) and sodium ion (Na$^+$), allowing reversible insertion/desertion reactions.[7–9]

For example, alloys, silicon, and metal anodes are prone to structural collapse due to large volume expansion during cycles, especially for SIBs.[10] By contrast, carbon-based materials with controllable capacity, excellent cycling stability, and cost-effectiveness are promising anode materials for LIBs and SIBs. However, commercial graphite as standard anode material for LIBs, always fails to be applied in SIBs because of the thermodynamically unstable Na-related graphite intercalation compounds.[11,12] Hard carbon is a promising anode material for SIBs, which accommodate Na$^+$ via surface adsorption in defect sites,[5,13] but its inferior capacity (200–300 mA h g^{-1})[6] due to the unsatisfactory active sites and ion-accessible surface area limited its development.[14] It is imperative to explore cost-effective and mechanically stable carbon-based anode materials for high-performance LIBs and SIBs.

Rational intrinsic structure design, such as a porous structure with abundant defects and active sites, is a viable approach to improving the capacity of batteries.[15] As a result, porous carbon (PC) anodes with tunable microstructure, diverse forms, and large specific surface areas, have garnered significant attention for their potential application in both LIBs and SIBs.[16–18] Natural biomass is the most common carbon source for preparing

Table 1. The electrochemical properties of as-reported carbon-based anodes for LIBs and SIBs.

Anode Material		Electrochemical performances	Reference
Lotus stem 1400 carbons	SIB	350 mA h g^{-1} (at 100 mA g^{-1} after 450 cycles)	[27]
Biomass of corn cobs (HCC)	SIB	300 mA h g^{-1} (at 74.4 mA g^{-1} after 100 cycles)	[29]
Mesoporous carbon (C)/tin (Sn)	LIB	574 mA h g^{-1} (at 20 mA g^{-1} after 15 cycles)	[30]
	SIB	295 mA h g^{-1} (at 20 mA g^{-1} after 15 cycles)	
Sulfonated pitch derived hard carbon	LIB	310 mA h g^{-1} (at 37.2 mA g^{-1} after 50 cycles)	[31]
sugarcane waste-derived hard carbon	SIB	323 mA h g^{-1} (at 50 mA g^{-1} after 500 cycles)	[32]
Cotton derived hollow structured carbon	LIB	450 mA h g^{-1} (at 100 mA g^{-1} after 150 cycles)	[33]
polyethylene terephthalate-derived carbon	SIB	178 mA h g^{-1} (at 100 mA g^{-1} after 140 cycles)	[34]
Poly tannic acid carbon rods	LIB	535 mA h g^{-1} (at 100 mA g^{-1} after 100 cycles)	[35]
Polyacrylonitrile nanofibers	LIB	390 mA h g^{-1} (at 100 mA g^{-1} after 100 cycles)	[36]
	SIB	200 mA h g^{-1} (at 100 mA g^{-1} after 100 cycles)	
N-rich carbon nanotubes	LIB	170 mA h g^{-1} (at 4000 mA g^{-1} after 5000 cycles)	[37]
	SIB	132 mA h g^{-1} (at 4000 mA g^{-1} after 5000 cycles)	
Hollow Carbon Nanospheres	LIB	310 mA h g^{-1} (at 372 mA g^{-1} after 200 cycles)	[38]
	SIB	200 mA h g^{-1} (at 50 mA g^{-1} after 100 cycles)	[39]
LPC	LIB	738 mA h g^{-1} (at 74.4 mA g^{-1} after 300 cycles)	This work
	SIB	460 mA h g^{-1} (at 74.4 mA g^{-1} after 300 cycles)	

PC, disordered, or hard carbon anodes, such as switchgrass,[19] peels,[20] etc. And diverse microstructure and morphology of carbon nanomaterials can be obtained by intentionally selecting biomass precursors with intrinsic structure. Additionally, various rhizomes, as Si-containing biomasses, can derive carbon materials doped with Si or SiO_2, which is beneficial to increasing capacity.[21] KOH is a commonly used chemical activation additive for creating edge sites in the preparation of PCs. The resultant carbon materials exhibit a well-defined micropore size distribution and an ultrahigh–specific surface area, which can reach up to thousands. However, PC anodes always show a significantly low initial Coulombic efficiency (ICE) and poor cycling stability for their fragile structure,[22] which can be improved by introducing coating or frame construction.

The lotus stems are a new kind of carbon precursor carrying abundant natural fiber[23] and a large number of naturally embedded soil elements at the molecular level, the K content is ≈2.5 wt% in the freeze-dried lotus stems that can activate biomass in situ during carbonization lead to a large specific surface area.[24] Furthermore, the abundant calcium oxalate (CaC_2O_4) plant crystals existing in the vacuoles of aquatic plant stems have a decomposition temperature of ≈800 °C,[25] and these crystals are often removed during the high-temperature carbonization process of bio-derived hard carbons, disregarding their potential as templates for preparing PC at lower temperatures. In addition, the breakdown of natural lotus silk and plant vacuoles, which contain a significant amount of cellulose, can result in the production of glucose. Then the glucose undergoes ring-closure condensation to form graphene quantum dots (GQDs) or pseudo-graphite structures.[26] Recently, hard carbon is synthesized via carbonizing lotus stems, delivering a high capacity of 350 mA h g^{-1} (in a current density of 100 mA g^{-1}) as anode for SIBs, however, the preparation temperature is up to 1400 °C and the as-prepared carbon exhibits a specific surface area of only 25.81 m^2 g^{-1}.[27] Furthermore, deliberately constructing inherent structural de-

fects can alter the chemical states on the surface of the carbon framework, thereby enhancing the durability of carbon-based materials.[15,28] Thus, it is vital to develop a successful plan that effectively integrates porosity and inherent flaws.

In this study, we present a simple and efficient approach for developing a lotus stem-derived PC (LPC) anode with abundant intrinsic defects through a self-template method. The resulting LPC anode demonstrates outstanding capacity, conductivity, and stability, making it a promising candidate as an anode for both LIBs and SIBs. The self-supporting porous structure in conjunction with embedded GQDs possesses abundant pores that facilitate the storage and transmission of Li$^+$ and Na$^+$. Additionally, this unique structure can modify the local charge distribution and reduce the diffusion path of ions, leading to a significant enhancement in the electrochemical performance of batteries. As shown in **Table 1** and the corresponding graphical representation of performance data (Figure S1, Supporting Information), despite being compared to the majority of hybrid or pure carbon anodes, the LPC electrodes still exhibit distinct advantages. The LIBs and SIBs based on the LPC anodes have high capacity (738 mA h g^{-1} and 460 mA h g^{-1} at 0.2 °C after 300 cycles, 1C≈372 mA h g^{-1}), superior long-term cyclic stability, and rate performance (440 mA h g^{-1} and 219 mA h g^{-1} at 5 °C after 1000 cycles), which are significantly higher than those of using graphite as anodes.

2. Results and Discussion

The XRD pattern of LPC is presented in **Figure 1**a. The broad peak located at around 23° and 43° is corresponding to the (002) and (100) planes of carbon, respectively,[40] representing the overall disordered and locally graphitized structure of PC.[41] The two broad peaks of the D-band at 1334 cm^{-1} and G-band at 1588 cm^{-1} in Raman patterns (Figure 1b) represent the existence of the defect and the E$_{2g}$ graphitic mode, respectively.[27,36] The N$_2$

**ADVANCED
SCIENCE NEWS**

www.advancedsciencenews.com
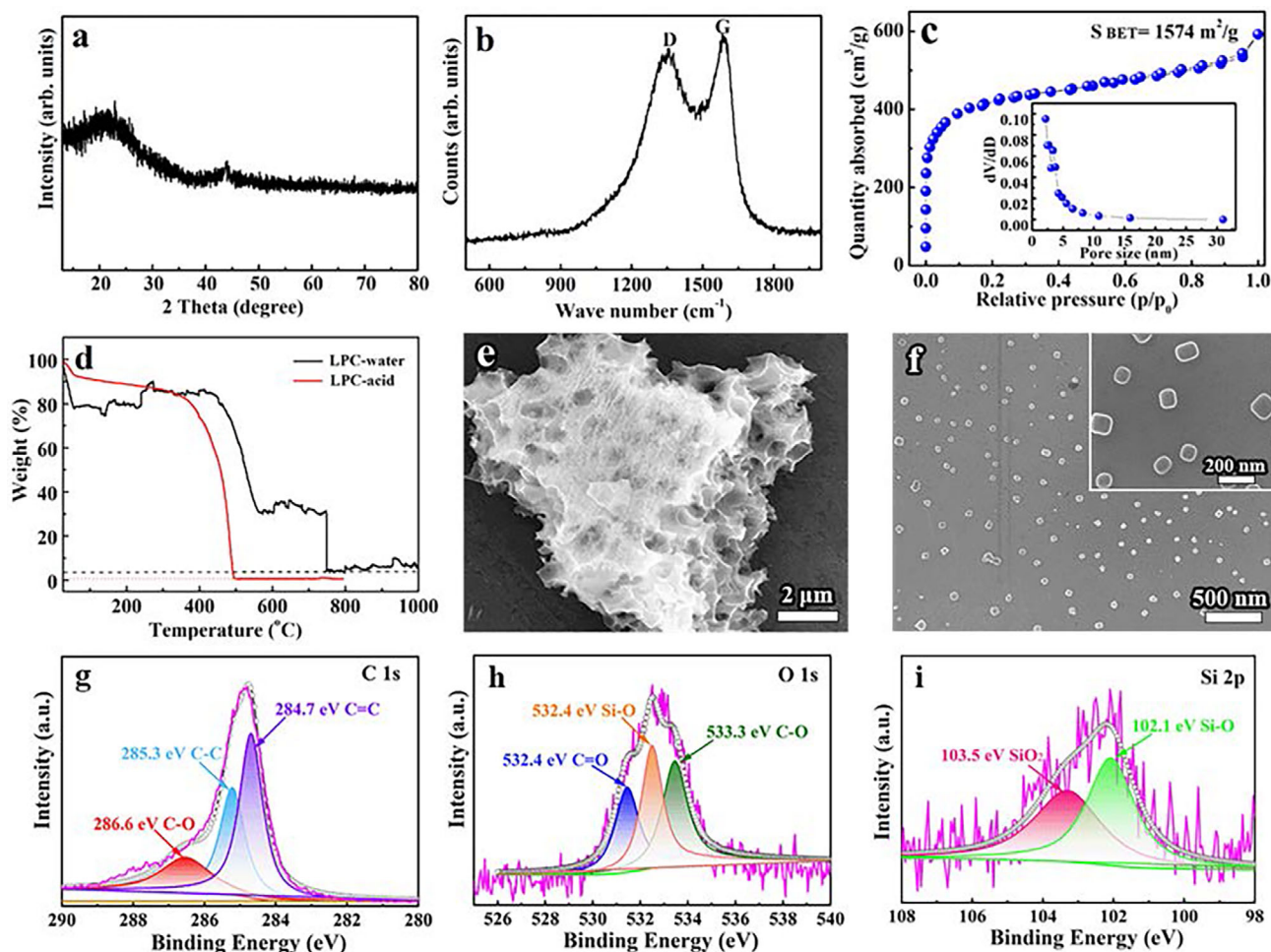
**small
methods**

www.small-methods.com

Figure 1. a) XRD patterns, b) Raman spectrum, and c) Nitrogen adsorption/desorption isotherms of the LPC samples. d) TGA curves of the LPC samples washed with deionized water and hydrochloric acid, respectively. e) The SEM image of the as-prepared LPC materials washed with deionized water and f) corresponding partially enlarged image located to CaC_2O_4. The high-resolution XPS spectra of C 1s (g), O 1s (h), and Si 2p (i) of the LPC materials.

adsorption/desorption isotherm of LPC in Figure 1c indicates that the as-prepared substances have a wealth of micropores and mesopores,[36] and the surface area is up to 1574 m^2 g^{-1}, symbolizing the high active sites. The Barrett–Joyner–Halenda (BJH) equation indicates that the pore size of LPC is mainly distributed in 3−5 nm (inset of Figure 1c) with a pore volume of 0.916 cm^3 g^{-1}. The surface functional group of the LPC is analyzed by Fourier transform infrared spectrum (FTIR, Figure S2, Supporting Information), the peaks at 1384 and 1640 belong to the C—H and C=O stretching vibration, respectively. The broad band in the range of 3300–3700 cm^{-1} is assigned to the —OH stretching vibration,[42] representing the huge number of outstanding hydroxyl groups on the surface of the LPC. The presence of hydrogen is more conducive to the extraction of oxygen, and the abundant oxygen species can provide more active sites for ion storage.[43] As a result, the distinctive architecture of LPC is beneficial to the effective contact of electrodes and electrolytes, facilitating the ions diffusion and the electrons transportation.

The thermogravimetric (TG) spectrum for the LPC sample neutralized with deionized water and hydrochloric acid is shown in Figure 1d. For the LPC washed with deionized water, the nat-

ural CaC_2O_4 template is not removed during the cleaning process compared to the case of hydrochloric acid, and a weight loss of 70% was observed after heating up to 600 °C and remained unchanged until 750 °C. There are two temperature regions in the process of losing weight. The first region ranges from 25 to 100 °C represents the weight loss caused by evaporating adsorbed water in the air,[44] and the second region ranges from 400 to 600 °C is associated with the loss of pyrolysis carbon. In addition, an apparent weight decay appears at ≈750 °C, corresponding to the decomposition of CaC_2O_4, following the reaction: CaC_2O_4 = $CaCO_3$ + CO. As a result, the content of CaC_2O_4 in PC materials is ≈25%. The higher content is also demonstrated by SEM images (Figures 1e,f) and the EDS elemental mappings in Figure S3 (Supporting Information), besides the as-prepared LPC, there are several well-dispersed square CaC_2O_4 crystals, which can serve as natural templates for the generation of braced frame structures between holes. In contrast, the CaC_2O_4 crystals in LPC samples washed with hydrochloric acid solution were well removed, showing no weight loss between 600 and 800 °C. The final sample content of ≈1% after heating to 800 °C corresponds to the existence of some intrinsic ingredients such as silicon (Si) and SiO_2,
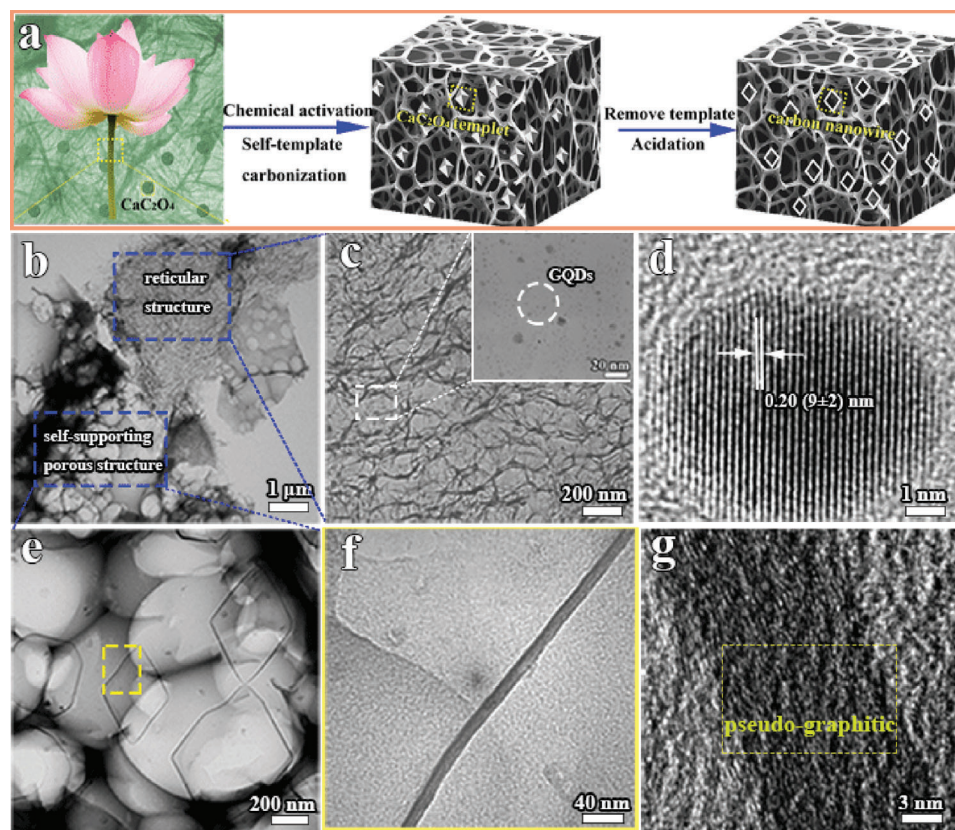
Figure 2. a) Schematic illustration for the synthesis procedures of LPC materials. b) Low-magnification TEM image of the LPC sample, c) high-magnification TEM image of LPC located in reticular structure with local magnification image of GQDs inset, and d) corresponding HRTEM image of GQDs. e) high-magnification TEM image of LPC located in a self-supporting porous structure, f) the local magnification image of the yellow squares in (e), and g) its HRTEM image.

which do not decompose at high temperatures or react with hydrochloric acid, its existence was also proved by corresponding EDS elemental mappings of LPC (Figure S4, Supporting Information).

The compositions and surface properties of LPC were further characterized by X-ray photoelectron spectroscopy (XPS) measurement. The C 1s spectrum (Figure 1g) is analyzed to identify three distinct peaks. The binding energies of 284.78, 285.3, and 286.6 eV, correspond to the C=C, C—C, and C—O,[45] respectively, the few oxygen contents enable LPC materials with more stable carbon skeleton.[43] Noted that some Si species are detected in the O 1s (Figure 1h) and Si 2p (Figure 1i) spectra, which serve as a key ingredient to improve the capacity of batteries.

The unique structural properties of the lotus stem locate in different parts including cell walls (Figure S5a, Supporting Information), plant crystals CaC_2O_4 (Figure S5b, Supporting Information), and natural silk fibers (Figure S5d, Supporting Information) are shown in TEM images. The prismatic and square structures embedded in plant cell walls are observed in Figure S5a,b (Supporting Information), and a lattice spacing of 0.29 nm is certificated by high-resolution TEM (HRTEM) (Figure S3c, Supporting Information), indicating its CaC_2O_4 crystal properties. It is well known that the main components of the cell wall are cellulose tthathat serves as a common carbon source, combined with the natural filaments that exist in the lotus stem, which

will partially hydrolyze into monosaccharides during hydrothermal. Following carbonizing the natural filaments at 700 °C for 2 h with KOH activation, the silk fibers will transform into a disordered mesh structure with some nanoparticles embedded (Figure S5e, Supporting Information), the lattice spacing of ≈0.21 nm proves that the nanoparticles are graphene quantum dots (GQDs) (FigureS2f, Supporting Information).[46] As a result, the natural fiber filaments and CaC_2O_4 crystals in the lotus stem are expected to produce unique carbon structures, as shown in **Figure 2**a.

As expected, the LPC presents a typical porous feature combined with some cross-linked network structure (Figure 2b), and many GQDs with a size of 2–5 nm distributed in a carbon net matrix (Figure 2c), showing a lattice spacing of 0.21 nm (Figure 2d), the conductivity of LPC anode can be significantly improved for the presence of porous network structure embedded with GQDs. Different from general porous carbon from chemical etching, there are some rhombic or square supporting frames embedded in the pore (Figure 2e,f) with a lattice spacing of ≈0.4 nm (Figure 2g), corresponding to the structure of pseudo-graphitic carbon, which is formed with intrinsic CaC_2O_4 template. The thickness of a loop–locked carbon nanowires framework (CNF) is ≈10 nm with an obvious lattice transition zone compared to an amorphous porous carbon frame. The larger interlayer space of CNF cannot only provide more interspace and more active
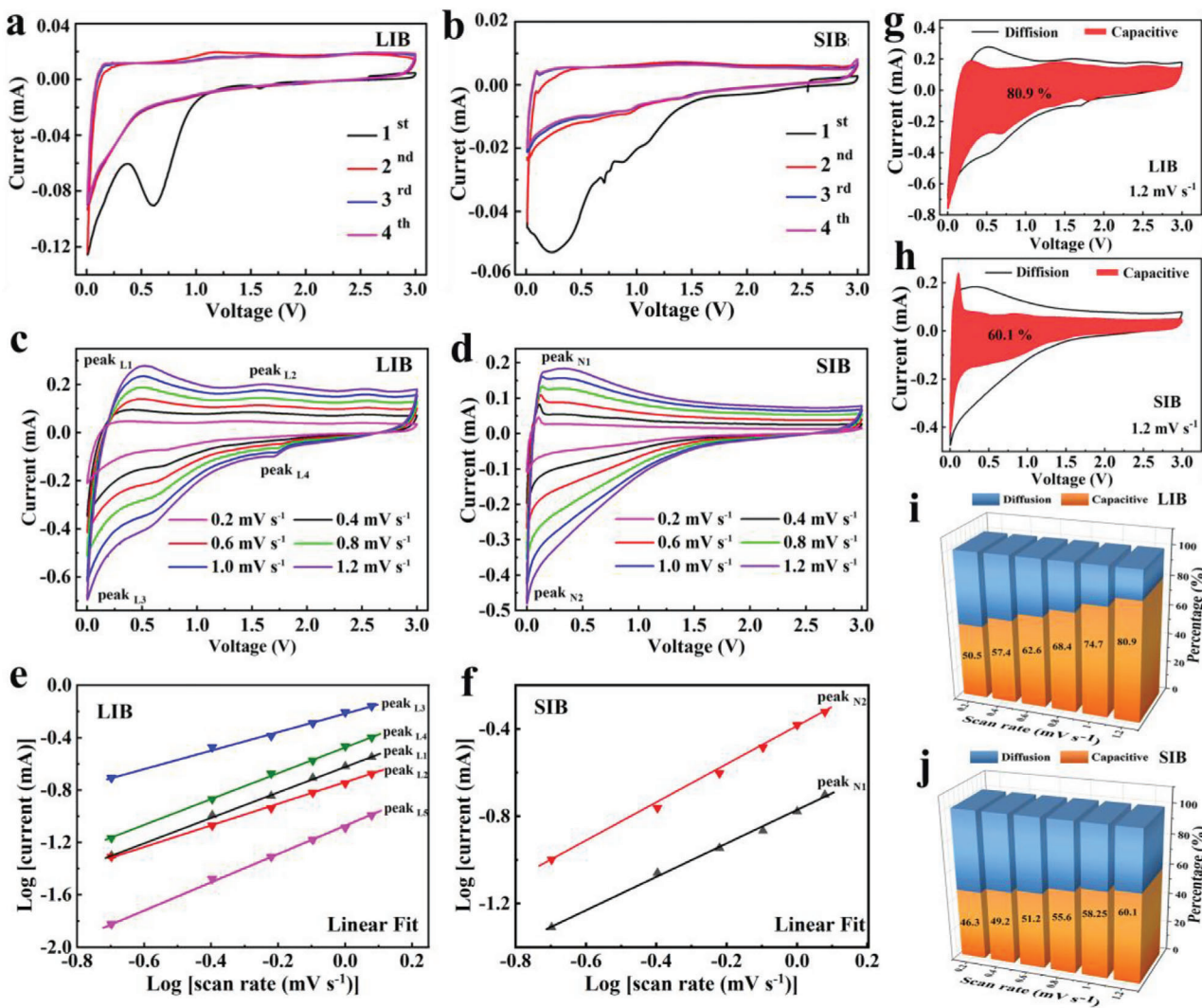
Figure 3. The cyclic voltammogram (CV) curves of the LPC anode in a) LIB and b) SIB tested between 0.01 V and 3.00 V at a scan rate of 0.1 mV s^{-1}, and different scan rates of 0.2–1.2 mV s^{-1} c) LIB and d) SIB. Plot of log (scan rate) versus log (peak current), as calculated from CV curves of e) LIB and f) SIB. Capacitive contribution in the CV curves of g) LIB and h) SIB at a rate of 1.2 mV s^{-1}. The trend of the capacitive contribution of i) LIB and j) SIB at different sweep rates.

sites for the insertion and extraction of Na$^+$ and Li$^+$ but effectively accommodate the volume expansion of anodes during the cycling process, leading to excellent electrochemical stability and higher capacity. By comparison, the LPC samples prepared at 800 °C (named LPC-1, Figure S6, Supporting Information) only show a porous structure with various of GQDs embedded, no CNF is found for the CaC$_2$O$_4$ template that has been directly decomposed during the high-temperature treating process. Furthermore, the hole size (1≈2 μm) of LPC-1 is much higher than LPC (50–500 nm) because the presence of intrinsic CaC$_2$O$_4$ template with a size of 30–100 nm in biochar precursors cannot only produce smaller pore structure but also reduce the pore-forming effect of KOH.

To gain a more comprehensive understanding of the mechanism and reaction kinetics of LPC electrodes in both LIBs and SIBs, CV measurements are carried out on the anode, as shown in **Figure 3**a,b. In the first discharging process of LIB, a broad peak is observed at ≈0.7 V (Figure 3a), which disappears in subsequent cycles, suggesting that there is an irreversible decomposition of electrolyte on the anode surface with the formation of solid electrolyte interphase (SEI) layer.[47] Furthermore, the small peak at 1.5–1.7 V is attributed to the reaction of Li$^+$ with some defects on the LPC anode.[48] The formation potential of the Na-related SEI layer in SIBs mainly corresponds to the two broad peaks centered at 0.3 and 0.8 V (Figure 3b), and the peak areas of SIB are smaller compared to LIB.[36,39]

The electrochemical kinetics mechanism of the LPC anode in LIB (Figure 3c) and SIB (Figure 3d) was investigated by testing CV curves at various scan rates ranging from 0.2 to 1.2 mV s^{-1}. Both the peak areas increased with increasing scan rates, demonstrating good rate performance. The identical shape of the curves further supports this conclusion. The total capacity is identified into pseudo-capacitance and diffusion-controlled contribution, which can be obtained by CV curve fitting at various rates. The
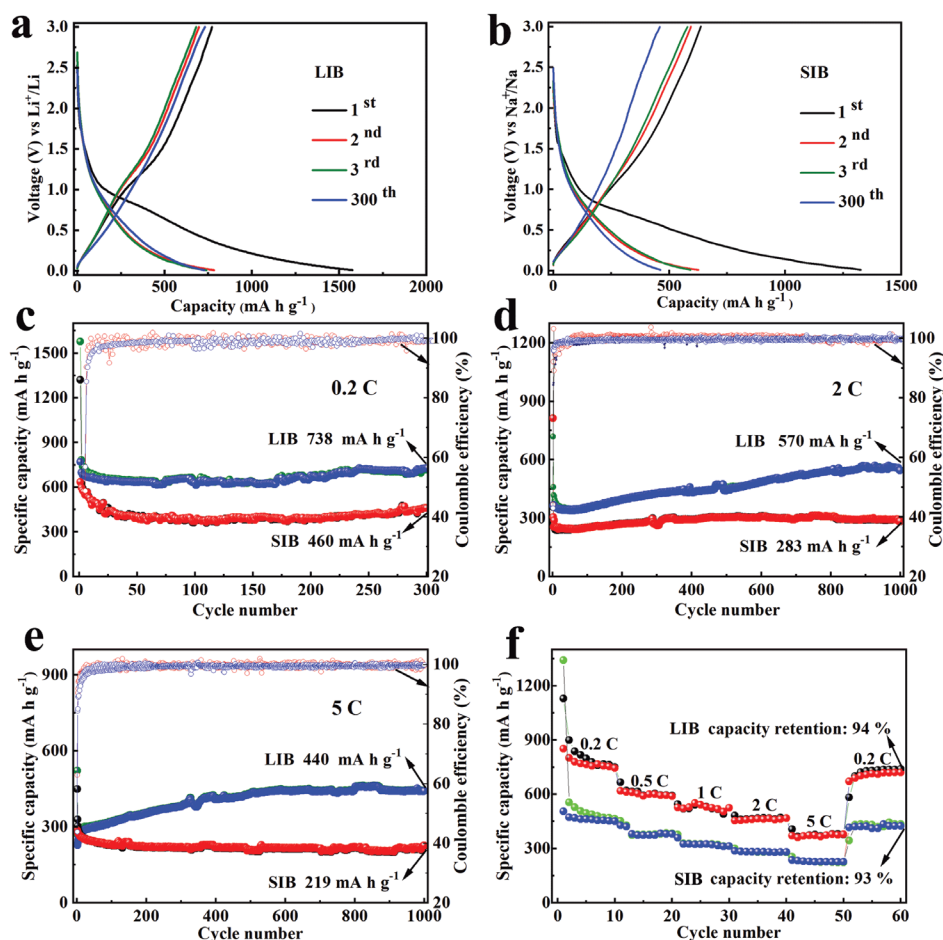
**ADVANCED
SCIENCE NEWS**

www.advancedsciencenews.com

**small
methods**

www.small-methods.com

Figure 4. Galvanostatic charge/discharge profiles of a) LIB and b) SIB were examined at a rate of 0.2 C (1 C ≈ 372 mA h g^{-1}). Cycle performances and CE of the LPC anodes in LIBs and SIBs at a rate of c) 0.2 C, d) 2.0 C, and e) 5.0 C, respectively. f) Rate performance at various current densities for the cells with LPC anodes.

current intensity (i) of the batteries as a function of scan rate (v) is plotted in Figure 3e following a power-law formula of $i = av^b$, where a and b are the fitting parameters. The value b near 1.0 corresponds to a surface-controlled process (capacitor behavior), while near 0.5 corresponds to a diffusion-controlled process (diffusion behavior).[43,49] Through linear fitting, the b values of peaks L$_1$–L$_5$ in LIB are 0.97, 0.82, 0.71, 0.99, and 1.08, in turn. And the b values of oxidation peak N$_1$ and reduction peak N$_2$ in SIB are 0.80 and 0.87, respectively. Both the b values of peaks are close to or even exceed 1, indicating a surface-controlled process either in LIBs or SIBs, such as adsorption on CNF or pores of LPC anodes.

The pseudocapacitive components at different scanning speeds were analyzed based on $i = k_1v + k_2v^{1/2}$, where k_1v ($k_2v^{1/2}$) corresponds to the capacitive process (diffusion process). The proportions of capacitive contributions of LPC anode in LIB (SIB) are 50.5% (46.3%), 57.4% (49.2%), 62.6% (51.2%), 68.4% (55.6%), 73.7% (58.2%), and 80.9% (60.1%) at scan rates of 0.2, 0.4, 0.6, 0.8, 1.0, and 1.2 mV s^{-1}, in turn. The proportions of pseudocapacitor contribution for LIB and SIB both increase with increasing scan rate, indicating the favorable cycling stability and rate performance of LPC anode.[49] The pseudocapacitor contri-

bution of LPC in LIB is higher concerning the case of SIB, for Na$^+$ has a larger ionic radius and poorer transmission dynamic than Li$^+$,[50] and the carbon-based materials normally have larger surface adsorption energies towards Li$^+$.[48]

The electrochemical impedance spectroscopy (EIS) in Figures S7 and S8 (Supporting Information) illustrates the charge transfer impedance, interface impedance, and ion diffusion resistance of the LPC and LPC-1 anodes before and after the 10th cycle in LIBs and SIBs, respectively. Before cycling, the high-frequency semicircle overlaps with the middle-frequency semicircle in LIB, but not in SIBs, meaning that the LPC anode possesses a less interface impedance with respect to the case of SIB.[51] After multiple charge/discharge cycles, both LIB and SIB exhibit reduced charge-transfer impedances and interface layer resistance due to the activation of the electrode and improved contact between the active material and electrolyte.[52] In contrast, the LPC-1 anodes show a larger impedance than the case of LPC whether before or after the 10th cycle (Figure S8, Supporting Information), indicating the unique structure of LPC can enhance ion transmissions and enhance the electrochemical performance of batteries. Calculated from the galvanostatic intermittent titration technique (GITT) curves (Figure S9, Supporting Information), both the Li$^+$
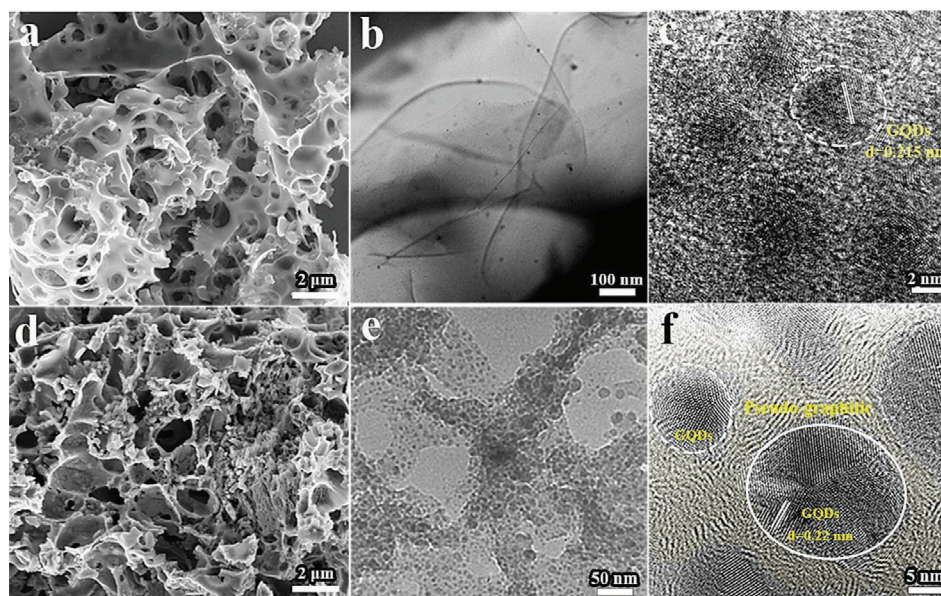
Figure 5. The a,d) SEM, b,e) TEM, and c,f) HRTEM images of LPC anode after the 500th discharging process at a rate of 2 C in a–c) LIB and d–f) SIB.

(10^{-7} to 10^{-10} cm^2 s^{-1}) and Na$^+$ (10^{-8} to 10^{-11} cm^2 s^{-1}) have a large diffusion coefficient in LPC anode, which is attributing to its unique porous structure and the good conductivity of GQDs.

The discharge/charge capacities of the LPC anode in LIB (**Figure 4**a) and SIB (Figure 4b) during the first cycle are 1575/773 mA h g^{-1} and 1325/636 mA h g^{-1}, respectively, having an ICE of 50% and 48%, the average CE are ≈98.5% and 98% during 300 cycles, indicating the excellent cycling stability of the LPC anode. Generally, the charging and discharging patterns in SIBs resemble those of LIBs, exhibiting a sharp incline and a noticeable plateau that correspond to the absorption of Li$^+$ or Na$^+$ into LPC. However, for the LPC-1 anode, the first discharge/charge capacities are 1691/809 mA h g^{-1} and 2894/1010 mA h g^{-1}, respectively, with an ICE of 47% (LIB-1) and 34% (SIB-1) (Figure S10, Supporting Information), indicating that there is a large consumption of electrolyte in the first cycling process. The average CE during 300 cycles is ≈98% (LIB-1) and 96.5% (SIB-1), respectively, which is lower than the case of LPC. The higher initial discharge/charge capacities of LPC-1 are attributed to its larger pore size compared to LPC, which generally leads to reduced reversibility and poor structural stability. However, CaC$_2$O$_4$ templet in LPC can produce both a smaller pore structure and a CNF framework with larger interlayer space and stable structure, which is favorable to improving the ICE and cyclability of batteries.

Figure 4c displays the cycle performances of the LPC anodes in LIB and SIB at 0.2 C. The reversible capacity can reach 738 mA h g^{-1} and 460 ma h g^{-1} after 300 cycles in LIB and SIB, respectively, the capacity attenuation of LIB during the first few cycles is attributed to the formation of SEI layers that take electrolyte as consumption.[16] Noted that when performed at high current densities (i.e., 2 C in Figure 4d and 5 C in Figure 4e), after the formation of SEI, the LIBs exhibit an increased reversible capacity from 350 mA h g^{-1} to 570 mA h g^{-1} at 2 C and 285 mA h g^{-1} to 440 mA h g^{-1} at 5 C after 1000 cycles, respectively, which is attributed to the fast structure activation of electrode as well as the

full infiltration of electrolyte.[53] Although the SIBs only maintain the reversible capacity of 283 and 219 mA h g^{-1} at the same condition, the value is significantly higher than the as-reported bio-carbon and even hard-carbon, for the SIBs anodes always suffer from a severe capacity decay at large current densities, which derived from the severe structural collapse caused by large-sized Na$^+$, and a substantial electrolyte consumption will happen in long-term cycling processes.

For example, the LPC-1 anode presents an obvious capacity fading at a high rate of 2 C (Figure S11b, Supporting Information) and 5 C (Figure S11c, Supporting Information) in SIBs, exhibiting the capacities of 242 and 146 mA h g^{-1} after 1000 cycling processes, respectively. Furthermore, the capacities of LPC-1 in LIBs and SIBs are all lower than that of LPC at various rates without no capacity increasing trend, and severe structural damage has become the major factor affecting capacity. Therefore, CNF plays an important role in maintaining structural stability and improving the capacity of LPC anodes. The rate performances of the LPC anodes at various current densities in SIBs and LIBs are shown in Figure 4f. The reversible capacity of LIB (SIB) at the rate of 0.2 C, 0.5 C, 1 C, 2 C, and 5 C is 740 (450 mA h g^{-1}), 589 (380 mA h g^{-1}), 525 (317 mA h g^{-1}), 456 (280 mA h g^{-1}), and 370 (226 mA h g^{-1}), respectively. When the current density drops to 0.2 C, the capacity retention rates reach ≈94% and 93%, respectively, which are higher than the LPC-1 anodes (93% for LIB and 80% for SIB, Figure S11d, Supporting Information). Noticeably, the structures and properties of LPC samples are not affected by the picking areas, which ensures the uniformity of the LPC anode materials for practical application (Figure S12, Supporting Information).

The favorable capacity retention and excellent stability of LPC anodes were ascribed to the structural stability of the self-supporting nanowires frame and the high reversible adsorption/desorption capability for lithium and sodium ions. Both the LPC anodes in LIB (**Figure 5**a) and SIB (Figure 5d) retain the original porous structure after 500 cycles at a rate of 2 C, and the CNFs

2300746 (7 of 9)

are still supported in the pores buffering the impact of Li^+/Na^+ on the carbon skeleton (Figure 5b). Noted that the interlayer space of GQD expands to ≈0.22 nm attributing to the combination of Li or Na ions (Figure 5c,f), enabling batteries with favorable electrical conductivity. And the adjacent pseudo-graphite carbon plays a key role in providing more active sites for ion migration and storage, especially for Na^+, resulting in an enhanced capacity and cycling stability for batteries. By contrast, the LPC-1 anodes suffer from serious structural damage after 500 cycles in LIB-1 (Figure S13a, Supporting Information) and SIB-1 (Figure S13b, Supporting Information), indicating that it is the CNFs enable LPC anode with high-rate performance and long cycling stability.

3. Conclusion

This study successfully fabricated a lotus stems-derived hybrid anode for Li and Na ion batteries using hydrothermal and chemical activation with a self-template method. The porous architecture with the carbon nanowire framework wrapped improves the utilization of the PC anode by allowing sufficient penetration of electrolytes and relieving volume expansion during charge/discharge cycles. In addition, the GQDs embedded within or clung to the surface of the porous carbon skeleton effectively improve the electrical conductivity, leading to an excellent electrochemical performance. The high reversible capacity (738 mA h g^{-1} for LIBs and 460 mA h g^{-1} for SIBs at 0.2 C after 300 cycles) and excellent long-term stability (440 mA h g^{-1} for LIBs and 219 mA h g^{-1} for SIBs at 5 C after 1000 cycles) have achieved both in LIBs and SIBs, which established its potential properties for the commercial field. This sustainable and cost-effective approach provides new perspectives for bio-carbon material engineering for second-ion batteries.

Supporting Information

Supporting Information is available from the Wiley Online Library or from the author.

Acknowledgements

Conflict of Interest

The authors declare no conflict of interest

Data Availability Statement

The data that support the findings of this study are available from the corresponding author upon reasonable request.

[1] I. Kovalenko, B. Zdyrko, A. Magasinski, B. Hertzberg, Z. Milicev, R. Burtovyy, I. Luzinov, G. Yushin, *Science* **2011**, *334*, 75.

[2] P. C. Rath, J. Patra, H. T. Huang, D. Bresser, T. Y. Wu, J. K. Chang, *ChemSusChem* **2019**, *12*, 1.

[3] G. Huang, Q. Kong, W. Yao, Q. Y. Wang, *J. Colloid Interface Sci.* **2023**, *629*, 832.

[4] J. Wang, X. Zhou, J. Tang, J. Yang, C. Luo, P. Cao, S. Fan, Y. Ma, *J. Energy Stor.* **2022**, *49*.

[5] W. Luo, F. Shen, C. Bommier, H. Zhu, X. Ji, L. Hu, *Acc. Chem. Res.* **2016**, *49*, 231.

[6] D. A. Stevens, J. R. Dahn, *J. Electrochem. Soc.* **2001**, *148*, A803.

[7] S. W. Kim, D. H. Seo, X. H. Ma, G. Ceder, K. Kang, *Adv. Energy Mater.* **2012**, *2*, 710.

[8] S. Hariharan, K. Saravanan, V. Ramar, P. Balaya, *Phys. Chem. Chem. Phys.* **2013**, *15*, 2945.

[9] H. Song, N. Li, H. Cuia, C. X. Wang, *Nano Energy* **2014**, *4*, 81.

[10] Y. K. Duan, Z. W. Li, S. C. Zhang, T. Su, Z. H. Zhang, A. J. Jiao, Z. H. Fu, *Molecules* **2023**, *28*, 5037.

[11] B. Jache, P. Adelhelm, *Angew Chem Int Ed Engl.* **2014**, *53*, 10169.

[12] Q. Liu, R. Xu, D. Mu, G. Tan, H. Gao, N. Li, R. Chen, F. Wu, *Carbon Energy* **2022**, *120*, 1.

[13] G. Hasegawa, K. Nakanishi, K. Kanamori, T. Abe, *ChemElectroChem* **2015**, *2*, 1917.

[14] W. J. Tian, H. Y. Zhang, X. G. Duan, H. Q. Sun, G. S. Shao, S. B. Wang, *Adv. Funct. Mater.* **2020**, *30*, 1909265.

[15] J. W. Zhu, S. C. Mu, *Adv. Funct. Mater.* **2020**, *30*, 2001097.

[16] X. C. Sun, J. L. Gao, C. Wang, X. Gao, J. S. Liu, N. Gao, H. D. Li, *Chem. Eng. J.* **2020**, *383*, 123198.

[17] X. Cheng, C. Tang, C. Yan, J. Du, A. Chen, X. Liu, L. Jewell, Q. Zhang, *Mater Today Bio* **2023**, *22*, 100321.

[18] T. Liu, X. Li, *Mater. Technol.* **2018**, *34*, 232.

[19] F. Zhang, Y. Yao, J. Wan, D. Henderson, X. Zhang, L. Hu, *ACS Appl. Mater.* **2017**, *9*, 391.

[20] J. Xiang, W. Lv, C. Mu, J. Zhao, B. C. Wang, *J. Alloys Compd.* **2017**, *701*, 870.

[21] Z. Zhao, M. Cai, H. Zhao, Q. Ma, H. Xie, P. Xing, Y. X. Zhuang, H. Yin, *ACS Sust. Chem. Eng.* **2022**, *10*, 5035.

[22] J. C. Wang, S. Kaskel, *J. Mater. Chem.* **2012**, *22*, 23710.

[23] M. Wu, M. Shuai, Q. Cheng, L. Jiang, *Angew. Chem., Int. Ed.* **2014**, *53*, 3358.

[24] Y. Zhang, S. Liu, X. Y. Zheng, X. Wang, Y. Xu, H. Q. Tang, F. Y. Kang, H. Yang, J. Y. Quan, *Adv. Funct. Mater.* **2017**, *27*, 1604687.

[25] Q. S. Fu, Z. X. Cui, Y. Q. Xue, *Eur Phys J Plus* **2015**, *130*, 212.

[26] W. Chen, D. Li, L. Tian, W. Xiang, T. Wang, W. Hu, Y. Hu, S. Chen, J. Chen, Z. Dai, *Green Chem.* **2018**, *20*, 4438.

[27] N. Zhang, Q. Liu, W. Chen, M. Wan, X. C. Li, L. Wang, L. H. Xue, W. X. Zhang, *J. Power Sources* **2018**, *378*, 331.

[28] L. Hou, W. Yang, B. Jiang, P. Wang, L. Yan, X. C. Zhang, G. Y. Huang, F. Yang, Y. F. Li, *Carbon* **2021**, *183*, 176.

[29] P. Liu, Y. Li, Y. Hu, H. Li, L. Chen, X. Huang, *J. Mater. Chem. A* **2016**, *4*, 13046.

[30] Y. H. Xu, Y. J. Zhu, Y. H. Liu, C. S. Wang, *Adv. Energy Mater.* **2013**, *3*, 128.

**ADVANCED
SCIENCE NEWS**

www.advancedsciencenews.com

**small
methods**

www.small-methods.com

[31] J. Zuo, Y. Guo, *Inter. J. Electrochem. Sci.* **2020**, *15*, 3196.

[32] K. H. Yu, X. R. Wang, H. Y. Yang, Y. Bai, C. Wu, *J. Energy Chem.* **2021**, *55*, 499.

[33] Y. Cheng, J. Huang, J. Li, H. Xie, Y. Wang, F. Yu, B. Shi, B. Liu, *Micro Nano Lett.* **2020**, *15*, 1095.

[34] D. Chen, K. Luo, Z. Yang, Y. Zhong, Z. Wu, Y. Song, G. Chen, G. Wang, B. Zhong, X. Guo, *Carbon* **2021**, *173*, 253.

[35] G. Huang, Q. Kong, W. Yao, Q. Wang, *J. Colloid Interface Sci.* **2023**, *629*, 832.

[36] J. Jin, Z. Q. Shi, C. Y. Wang, *Electrochim. Acta* **2014**, *141*, 302.

[37] S. Zhong, H. Z. Liu, D. H. Wei, J. Hu, H. Zhang, H. S. Hou, M. Peng, G. H. Zhang, H. G. Duan, *Chem. Eng. J.* **2020**, *395*, 125054.

[38] K. Tang, R. J. White, X. Mu, M. M. Titirici, P. A. Aken, J. Maier, *ChemSusChem* **2012**, *5*, 400.

[39] K. Tang, L. J. Fu, R. J. White, L. H. Yu, M. M. Titirici, M. Antonietti, J. Maier, *Adv. Energy Mater.* **2012**, *2*, 873.

[40] Y. M. Li, Y. S. Hu, M. M. Titirici, L. Q. Chen, X. J. Huang, *Adv. Energy Mater.* **2016**, *6*, 1600659.

[41] D. Wang, K. H. Tian, J. Wang, Z. Y. Wang, S. H. Luo, Y. G. Liu, Q. Wang, Y. H. Zhang, A. M. Hao, T. F. Yi, *Rare Met.* **2021**, *40*, 2464.

[42] C. X. Yu, Y. Li, Z. H. Wang, X. R. Wang, Y. Bai, C. Wu, *Rare Met.* **2022**, *41*, 1616.

[43] M. Song, Z. Yi, R. Xu, J. Chen, J. Cheng, Z. Wang, Q. Liu, Q. Guo, L. Xie, C. Chen, *Energy Storage Mater.* **2022**, *51*, 620.

[44] Q. S. Zhao, H. Xie, H. Ning, J. L. Liu, H. Zhang, L. Wang, X. B. Wang, Y. L. Zhu, S. Y. Li, M. B. Wu, *J. Alloys Compds.* **2018**, *737*, 330.

[45] Z. Wang, K. Dong, D. Wang, S. Luo, Y. Liu, Q. Wang, Y. Zhang, A. Hao, C. Shi, N. Zhao, *J. Mater. Chem. A* **2019**, *7*, 14309.

[46] W. W. Yao, J. Ren, J. Mao, L. Wang, Z. W. Chen, D. Y. Pan, M. H. Wu, Z. Li, *J. Electrochem. Soc.* **2020**, *167*, 060513.

[47] Y. L. Cao, L. F. Xiao, X. P. Ai, H. X. Yang, *Electrochem. Solid S. T.* **2003**, *6*, A30.

[48] Y. P. Song, H. D. Li, L. Y. Wang, D. C. Qiu, Y. B. Ma, K. Pei, G. T. Zou, K. F. Yu, *Chem. Commun.* **2016**, *52*, 10497.

[49] Z. Yuan, L. Wang, D. Li, J. Cao, W. Han, *ACS Nano* **2021**, *15*, 7439.

[50] V. Palomares, P. Serras, I. Villaluenga, K. B. Hueso, J. Carretero-González, T. Rojo, *Energy Environ. Sci.* **2012**, *5*, 5884.

[51] S. M. Abbas, S. T. Hussain, S. Ali, N. Ahmad, N. Ali, S. Abbas, *J. Mater. Sci.* **2013**, *48*, 5429.

[52] X. Y. Shen, D. B. Mu, S. Chen, R. Huang, Wu, F., *J. Mater. Chem. A* **2014**, *2*, 4309.

[53] J. L. Cui, F. P. Cheng, J. Lin, J. C. Yang, K. Jiang, Z. S. Wen, J. C. Sun, *Powder Technol.* **2017**, *311*, 1.